Geophys. J. Int. (2003) **155,** 111–125

Fault compaction and overpressured faults: results from a 3-D model of a ductile fault zone

D. D. Fitzenz[1,*] and S. A. Miller[2]

[1] *Geology Institute, Swiss Federal Institute of Technology, Zürich, Switzerland. E-mail: fitzenz@erdw.ethz.ch*
[2] *Geophysics Institute, Swiss Federal Institute of Technology, Zürich, Switzerland. E-mail: miller@erdw.ethz.ch*

Accepted 2003 April 3. Received 2003 March 17; in original form 2002 June 24

SUMMARY

A model of a ductile fault zone is incorporated into a forward 3-D earthquake model to better constrain fault-zone hydraulics. The conceptual framework of the model fault zone was chosen such that two distinct parts are recognized. The fault core, characterized by a relatively low permeability, is composed of a coseismic fault surface embedded in a visco-elastic volume that can creep and compact. The fault core is surrounded by, and mostly sealed from, a high permeability damaged zone. The model fault properties correspond explicitly to those of the coseismic fault core. Porosity and pore pressure evolve to account for the viscous compaction of the fault core, while stresses evolve in response to the applied tectonic loading and to shear creep of the fault itself. A small diffusive leakage is allowed in and out of the fault zone. Coseismically, porosity is created to account for frictional dilatancy. We show in the case of a 3-D fault model with no in-plane flow and constant fluid compressibility, pore pressures do not drop to hydrostatic levels after a seismic rupture, leading to an overpressured weak fault. Since pore pressure plays a key role in the fault behaviour, we investigate coseismic hydraulic property changes. In the full 3-D model, pore pressures vary instantaneously by the poroelastic effect during the propagation of the rupture. Once the stress state stabilizes, pore pressures are incrementally redistributed in the failed patch. We show that the significant effect of pressure-dependent fluid compressibility in the no in-plane flow case becomes a secondary effect when the other spatial dimensions are considered because in-plane flow with a near-lithostatically pressured neighbourhood equilibrates at a pressure much higher than hydrostatic levels, forming persistent high-pressure fluid compartments. If the observed faults are not all overpressured and weak, other mechanisms, not included in this model, must be at work in nature, which need to be investigated. Significant leakage perpendicular to the fault strike (in the case of a young fault), or cracks hydraulically linking the fault core to the damaged zone (for a mature fault) are probable mechanisms for keeping the faults strong and might play a significant role in modulating fault pore pressures. Therefore, fault-normal hydraulic properties of fault zones should be a future focus of field and numerical experiments.

Key words: earthquake mechanics, fault models, permeability, seismicity, viscoelasticity.

1 INTRODUCTION

The critical role of fluids in the behaviour of fault systems requires that fault-zone hydraulics be modelled realistically. The objective of this work is to incorporate field- and laboratory-based observations (e.g. architecture, rheology, etc.) into a physics-based 3-D forward earthquake generation model (Fitzenz & Miller 2001, referred to herein as FM01).

Sibson (1992) was the first to advocate complex interactions between stress cycling, the creation and destruction of permeability, and fluid flow assuming a rapid resealing of the earthquake-related fault permeability increase. Blanpied *et al.* (1992) developed the idea of rapid sealing with shear-induced compaction and subsequent pore pressure increase as an instability mechanism for earthquakes, while Rice (1992) proposed the existence of deep fluid sources to maintain high pore pressures in fault zones.

Following these conceptual models that account for the influence of fluids in faulting, numerous laboratory investigations focused on the behaviour of a simulated fault gouge. Studies of the effects of slip, slip rate and shear heating on the friction of granite (Blanpied *et al.* 1998) showed an influence of fluids on fault stability at high strain rates (e.g. the competition between velocity strengthening and velocity weakening due to thermal pressurization of a poorly drained pore fluid). Zhang *et al.* (2001) tested the anisotropic alignment of clay shape fabrics as a candidate for focusing fluid flow along fault

*Now at: USGS, Menlo Park, USA. E-mail: fitzenz@usgs.gov

zones and for maintaining high pore pressures in clay-rich rocks. Adding to the debate, they show that fabric anisotropy alone is not enough to cause focused fluid flow along natural fault zones.

Studies on core samples and downhole measurements from drilling through the Nojima fault (Japan) 1 year after the Kobe earthquake (1995) yielded a new insight into the fault-zone structure and hydraulic processes and timescales (e.g. Open-File Report 00-29 Tanaka *et al.* 2001). Field and laboratory studies of the Median Tectonic Line (Japan) describe the internal structure and permeability of a large structurally complex fault zone (Wibberly & Shimamoto 2003). Pre- and co-seismic magnetotelluric surveys in the North Anatolian Fault system (Izmit earthquake, 1999, Honkura *et al.* 2000) allowed inferences on the link between fluid content and fault strength. A strong zone in the hypocentral area of the Izmit (1999, Turkey) earthquake is characterized by a high-resistivity zone. New theoretical developments derived from field observations at the San Gabriel Fault provided insight into the kinetics of crack-sealing, intergranular pressure solution and compaction around active faults (Renard *et al.* 2000; Gratier *et al.* 2003). The kinetics of crack sealing is shown to mainly control the fluid pressure and fluid flux changes on the faults. Zones of high pressure are predicted, due to fluid inflow from depth.

Modelling efforts that investigated the different aspects of the involvement of fluids in faulting include Sleep & Blanpied (1992, 1994) and Sleep (1995). They proposed a 1-D fault model mostly sealed from the country rock in which pore pressures follow the seismic cycle. In their model, overpressures are generated via ductile creep during interseismic periods and drop to hydro- or subhydrostatic levels after a rupture. Segall & Rice (1995) developed a model for dilatancy and compaction within the framework of a rate- and state-dependent friction law and a spring slider model and showed that pore pressure plays a major role in stick-slip instability. Miller *et al.* (1996) proposed a 2-D fault model for an elastic half-space including large-scale tectonic loading and using a cellular automaton scheme for the monitoring of pore pressures. Henderson & Maillot (1997) presented a 2-D model of the fluid flow within a tabular fault zone and the competing effects of diffusivity and compaction rate on the seismic cycle. Models of the dynamic triggering (Harris & Day 1999), static stress triggering (Stein *et al.* 1997), post-seismic deformation (Pollitz *et al.* 2001) and forward fault interaction models (Robinson & Benites 1995, 1996) typically ignore fluid processes other than poroelasticity. Earthquake simulations include asperity models (Ben-Zion & Rice 1993) or synthetic rupture history models (Ward 1997). The role of fluids in swarm generation has been investigated by Yamashita (1999), and a forward model driven by crustal fluids was developed by Miller *et al.* (1999) and generalized to 3-D interacting faults by Fitzenz & Miller (2001) (FM01). They show how pore pressures influence the complexity of the seismic process and the earthquake cycle, but are limited in their analysis by a lack of constraints on the hydraulic properties within the framework of a forward 3-D model.

In this study, we investigate a forward model of a ductile tabular fault zone embedded in an elastic half-space. The model combines 3-D large-scale tectonic loading and stress transfer with a detailed handling of the hydraulics of a ductile fault zone. The stress state of the model is complex, with at least four degrees of freedom in stress space. These include the normal stress and shear stress increase due to tectonic loading, shear stress decrease due to shear creep slip and pore pressure increase due to ductile compaction. Pore pressure changes via poroelastic effects add an additional change in the stress state. The new fault-zone conceptual model is chosen after field and borehole observations of active crustal faults (Tanaka *et al.* 2001). No fluid source boundary condition is prescribed at the downward continuation of the fault. After deriving the system of equations necessary to include a thin vertical viscous layer in the 3-D elastic half-space, we extend the shear creep and ductile compaction model of Sleep & Blanpied (1992, referred to hereafter as SB92) to 3-D. We show that the pressure dependence of the fluid compressibility plays a key role in the pore pressure drops to hydro- or subhydrostatic levels after seismic events shown in SB92. When extended to 3-D, with more realistic loading and fault-zone hydraulics, the results show that a mostly overpressured fault below 6 km depth organizes into compartments of varying pore pressures, complex stress states and seismic and creep slip patterns. We discuss implications of the SB92 model in 3-D, the creep slip distribution, the development of overpressures and the role of the pressure dependence of the compressibility as a regulator of model pore pressures. Alternatives such as flow in the direction perpendicular to the fault strike are also discussed.

2 CONCEPTUAL MODEL OF FAULT-ZONE HYDRAULICS AND DEFORMATION

The conceptual fault-zone structure and architecture that we aim to simulate (Fig. 1) is a simplification of the structure of the Nojima fault inferred from core observations (Tanaka *et al.* 2001). The fault is characterized by two distinct zones: a relatively low-permeability fault core consisting of a coseismic fault surface embedded in a zone composed of breccia and/or cataclasite, or gouge and a high-permeability damaged zone surrounding the core. Rawling *et al.* (2001) review permeability data for contrasting types of fault zones and show, in the case of a granitic protolith, permeability ratios of 10^3 and 10^{-3}, for the damage zone and the fault core, respectively, with respect to the intact rock. Chester *et al.* (1993) proposed episodic self-sealing of the fault-bounding rocks as one factor allowing for the generation and maintenance of elevated fluid pressures for the studied segments of the San Andreas fault. For a quasi-impermeable narrow seal between the fault core and the surrounding rocks, a small diffusive leakage out of the fault zone during interseismic periods is expected.

Field evidence shows negligible re-orientation of planar structures predating the brittle faulting episode except very near or within the fault core (Chester *et al.* 1993). This suggests that only a negligible component of the total slip on the fault is accommodated by simple shear in the damage zone and that most coseismic displacement occurs along the fault core. In addition, the damaged zone must not necessarily be symmetric with respect to the slipping plane. That is, the damage zone can exist either on both sides (as shown on Fig. 1) or on only one side of the fault core.

Time-dependent processes such as shear creep and ductile compaction can occur during interseismic periods even on mostly seismic faults (Chester *et al.* 1993). Sleep & Blanpied (1992) demonstrated that shear creep mildly reduces shear stress, whereas ductile compaction can significantly increase pore pressure in the fault zone (and decrease the frictional strength). As seismic slip initiates and propagates along the fault plane, part of the elastic energy release is used for porosity creation (e.g. frictional dilatancy, Marone *et al.* 1990). Whether these new cracks and pores are rapidly filled with fluids is still unknown. However, seismic slip can hydraulically connect parts of the fault previously sealed from each other, thus initiating flow.

Stress transfer occurs at wave speeds while flow occurs within diffusive timescales. Therefore, pore pressures can start equilibrating

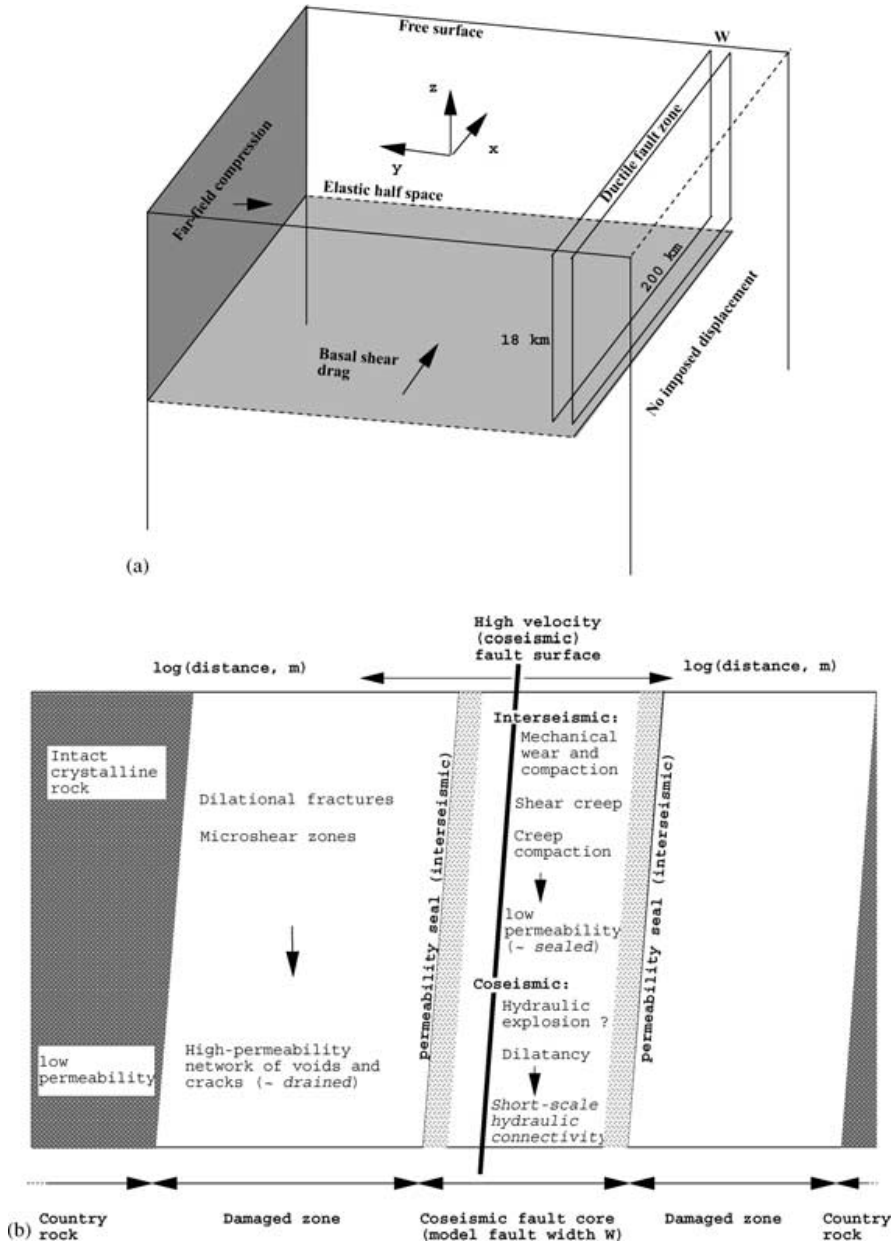

Figure 1. Model fault. (a) Model geometry, tectonic loading and boundary conditions. We consider the case of a vertical finite fault model consisting of a sealed tabular ductile body of width W embedded in an elastic country rock (half-space). The tectonic loading is performed via both a basal shear drag (30 mm yr^{-1} at 20 km depth) and a far-field compression (3 mm yr^{-1}). We impose a constant hydraulic head condition at the top of the fault. (b) Structure of the model fault zone (adapted after Tanaka *et al.* 2001). Slip occurs on very narrow fault surfaces embedded in a zone of width W that increases with the total slip. This zone has a low permeability, roughly between 10^{-20} and 10^{-18} m^2 during interseismic periods and up to 10^{-15} m^2 coseismically. The (drained) damaged zone is not part of the model fault zone. A small leakage to out of the fault core is allowed.

only after the fault is stable with respect to its total stress state, and the rupture propagation itself is considered to be undrained. Undrained poroelastic effects within the cells are passed on to pore pressures without delay. The width of the fault zone increases with total seismic slip (Scholz 1990; Yamashita 1999) because of the crack formation (and possibly hydraulic fracturing Tanaka *et al.* 2001). We consider that the top of the fault is hydraulically connected to the surface and therefore has a constant hydraulic head. This can result in water outflow when the rupture reaches the surface (e.g. pore pressure redistribution). It could potentially result in water inflow if the pore pressure within the fault core dropped below hydrostatic, which never happened in our simulations.

Limitations of the approach

According to soil mechanics deformation experiments, the initial consolidation state of the fault core has a significant influence on its initial type of deformation under shearing. Underconsolidated material (e.g. loosely packed sand) will have a tendency to compact, whereas overconsolidated material (e.g. dense sand) will initially dilate (Morrow & Byerlee 1989). It could be argued that the state of

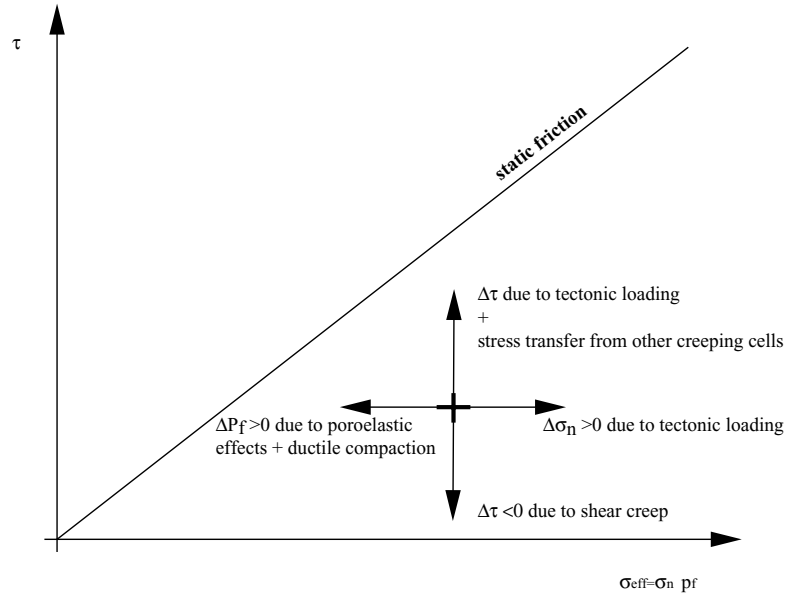

Figure 2. Degrees of freedom in the Mohr stress space to consider when calculating the exact time step to the next failure of a cell in the model fault system. During interseismic periods, shear stress decreases on a cell due to shear creep and increases from both tectonic loading and stress transfer from other creeping cells, whereas the effective stress increases from normal stress increase and decreases due to pore pressure increase (from poroelastic effects and creep compaction).

consolidation of the fault core is likely to vary within the earthquake cycle. However, whether faults are underconsolidated right after an earthquake and overconsolidated at the end of the interseismic period is unknown, and therefore not included in the model.

Another phenomenon commonly observed in soil mechanics tests and described in studies of compaction during frictional sliding on faults containing gouge (Morrow & Byerlee 1989) is time-dependent compaction associated with strengthening, shown to be significant mostly at timescales larger than 1000 to 10 000 s (their fig. 9). The timescale of this process is long compared with that of seismic events. This happens during 'hold' experiments when the piston stays stationary. There is also good evidence (guided waves, Li *et al.* 2001; Li & Vidale 2001) that faults are left in a more dilatant state following an earthquake. Although the fault-healing rate as determined by a time-dependent wave velocity analysis can be quantified in terms of a compaction rate (Li *et al.* 1998; Li & Vidale 2001), it still leaves open the question of whether or not the fault will be overconsolidated just prior to the next earthquake. Having no better description of it, we simply consider that it either does not apply to mature faults or is included in the interseismic ductile compaction term mentioned above.

Other simplifications include the zero-cementation rupture criterion (i.e. the fault already exists when the simulation starts) and the absence of a friction increase in log (t) during interseismic periods.

3 THE NUMERICAL MODEL

As in the original model (FM01), faults of any strike and geometry can be considered. However, we concentrate in this study on the case of a vertical strike-slip fault to be able to compare the results with the 1-D case of Sleep & Blanpied (1992). The model fault consists of a matrix of computational cells (subfaults) representing rectangular dislocations and discrete sealed fluid pressure compartments in a deforming elastic half-space. Tectonic loading increases shear stress, normal stress and pore pressure (through poroelasticity) along the fault planes, while pore pressures increase through poroelastic effects and compaction within the faults. This results in four degrees of freedom in the Mohr diagram (Fig. 2), and we can therefore expect a complex stress state and seismic behaviour. When a cell reaches the Coulomb failure stress, we use Okada's (1985, 1992) analytical solutions to calculate slip on this cell and the stress changes on all other cells of the faults. The fluid-related processes are accounted for via undrained poroelasticity, a source term, frictional dilatancy and a toggle switch in permeability allowing an instantaneous equilibration of pore pressures over the entire slipped area at the end of a seismic event (see Fitzenz & Miller 2001 for more details). Differences with FM01 include an explicit calculation of the compaction rate, creep slip, a total slip-dependent fault-zone width, and an incremental coseismic pore pressure redistribution. These are presented in the next sections.

The new pore pressure state after equilibration can change the Coulomb failure stress and trigger slip on other cells during the same event. Tectonic loading is decomposed into basal shear drag parallel to the plate boundary with a 30 mm yr^{-1} plate velocity, and a ridge push, or gravity push (e.g. of the Sierra Nevada mountains on the San Andreas fault system) compression approximated by a vertical dislocation surface applied at the far-field boundary resulting in fault-normal compression rates in the model space of 3 mm yr^{-1} (Argus & Gordon 1991 proposed 2 mm yr^{-1}, -1 to $+5$ mm yr^{-1} from interferometry surveys).

Even though the lower bound of the magnitude range of the generated events is kept about $M_w = 4$ because of the cell size, the hydraulic processes are handled so that the resulting pore pressure is mostly cell-size independent as described in Section 4 and discussed in Section 5.

3.1 A viscoelastic fault core: shear creep and compaction rate

The properties of the subfaults (e.g. porosity, compressibility, Skempton's coefficient, friction coefficient, pore pressure) are now

explicitly defined as those of the coseismic fault core. We assume that slip occurs on very narrow fault surfaces embedded in a highly deformed zone of width W. Chester *et al.* (1993) observed on exhumed faults of the San Andreas fault system that both the total fault-zone thickness, and the fault core thickness scale with displacement. Following Yamashita (1998), the fault core widens with the total accumulated slip at any given location $\mathbf{x}$ on the fault by

$$W(\mathbf{x}) = \zeta \sum_m D_m(\mathbf{x}) + W_0, \qquad \zeta \in [0.001, 0.1], \tag{1}$$

where W_0 is the initial width, D_m is the total seismic slip of the subfault during event m and is summed for all the past seismic (brittle) events at a given time. The parameter ζ is interpreted as a wear rate. When slip and thickness data are collected for faults in crystalline rocks (Scholz 1990), the cloud of points lies between lines of $\zeta = 0.001$ and 0.1, and we chose $\zeta = 0.05$.

3.1.1 Applying a 1-D formalism in a 3-D case

Following the model of Sleep & Blanpied (1992), we consider a viscoelastic fault core of width $W$and down-dip extension within the seismogenic layer embedded in an elastic half-space. The introduction of this thin viscous vertical layer requires the rewriting of the set of equations for modelling creep slip and pore pressure increase rates. Consider a tabular viscous fault core, infinite along strike (x-axis) and in depth (z-axis), of width W(y-axis) embedded in an elastic country rock (Fig. 3). A shear displacement u_x is applied along $x$on the elastic body over an effective width L. Static equilibrium requires continuity of both shear stress and normal stress across the fault core. Therefore, the shear stress at the interface between the country rock and the fault core is given by $\sigma_{xy} = G\frac{\partial u_x}{\partial y}$. This is equivalent to $\sigma_{xy} = G\frac{d_1 - d_2 - d_f}{L}$, where $G$is the rigidity of the country rock, d_1 and d_2 are the displacements imposed on both sides of the elastic body and d_f is the creep displacement along the fault.

The creeping rate along the fault for a linear viscous medium of shear viscosity η is $\dot{d}_f = \int_W \frac{\sigma_{xy}}{\eta} dy$, where $W$is the fault-zone width and $\dot{d}_f$ is the slip rate along the fault. Thus,

$$\dot{d}_f = G\frac{d_1 - d_2 - d_f}{L}\int_W \frac{dy}{\eta}. \tag{2}$$

The relationship between the total stress and the (inelastic) compaction rate for a ductile fault core is

$$K\frac{D\phi_{pl}}{Dt} = P_f - P_T, \tag{3}$$

where ϕ is the porosity of the fault core, P_f is the pore pressure, P_T is the total applied external stress and D/Dt is the material derivative ($\frac{D}{Dt} = \frac{\partial}{\partial t} + \mathbf{v}_s \cdot \nabla$, $\mathbf{v}_s$ being the velocity of the solid). K is the bulk viscosity (in units of Pa s) (Sleep & Blanpied 1992) and relates the deformation to the deformation rate (Barnes *et al.* 1993 p. 169) (see the calculation in Section 3.1.2).

The conservation equations for the solid and the liquid are

$$\frac{\partial \rho_f \phi}{\partial t} + \nabla \cdot (\phi \rho_f \mathbf{v}_f) = 0 \tag{4a}$$

$$\frac{\partial \rho_s (1-\phi)}{\partial t} + \nabla \cdot [(1-\phi)\rho_s \mathbf{v}_s] = 0, \tag{4b}$$

where ρ_f, $\mathbf{v}_f$ and ρ_s, $\mathbf{v}_s$ are the densities and the velocities of the fluid and the solid, respectively. Assuming an incompressible solid matrix (e.g. ρ_s is constant), and by adding eq. (4):

$$\nabla \cdot (\phi \mathbf{v}_f + (1-\phi)\mathbf{v}_s) + \frac{\phi}{\rho_f}\frac{\partial \rho_f}{\partial t} = 0 \tag{5a}$$

$$-\frac{\partial \phi}{\partial t} + \nabla \cdot [(1-\phi)\mathbf{v}_s] = 0. \tag{5b}$$

Darcy's law is given by

$$\phi(\mathbf{v}_f - \mathbf{v}_s) = -\frac{k}{\mu_f}(\nabla P_f - \rho_f \mathbf{g}), \tag{6}$$

where k is the permeability within the fault core, g is the acceleration due to gravity and μ_f is the fluid viscosity.

The second term of eq. (5a) can be expressed using the fluid compressibility $\beta_f = \frac{1}{\rho_f}\frac{\partial \rho_f}{\partial P}$ as $\beta_f \frac{\partial P_f}{\partial t}\phi$. The time derivative of the porosity can be decomposed as an inelastic (see eq. 3) and an elastic compaction term. The latter is a function of the compressibility of the pores $\beta_\phi = \frac{1}{\phi}\frac{\partial \phi}{\partial P_f}$, the porosity, and the derivative of the pore pressure. Developing the divergence of the product and substituting into eq. (5):

$$\nabla \cdot \left[-\frac{k}{\mu_f}(\nabla P_f - \rho_f g)\right] + \phi\beta_f \frac{\partial P_f}{\partial t} = -\nabla \cdot (\mathbf{v}_s) \tag{7a}$$

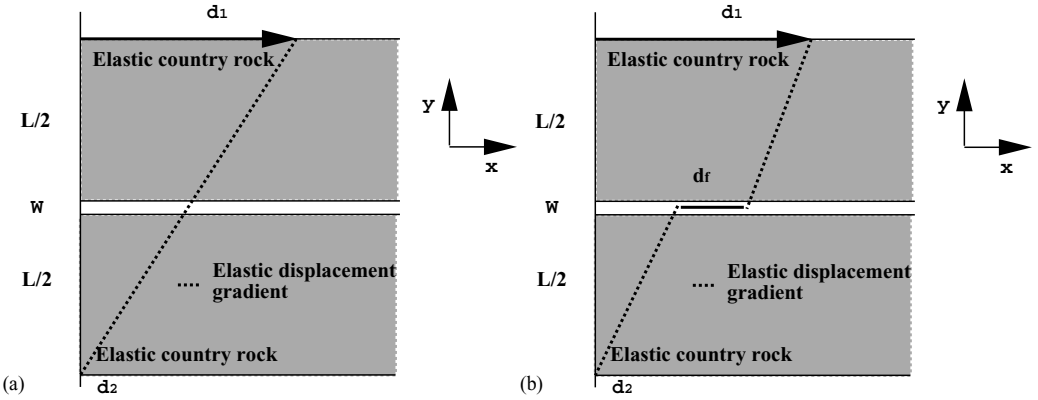

Figure 3. Geometry and boundary conditions (map view) between the tabular sealed ductile fault zone of width $W$and the country rock. $L$is the effective width of the region that deforms elastically. The displacements imposed at the boundaries are d_1 and d_2 in the general case discussed in Section 3.1. (a) Case where no slip occurs in the fault zone; (b) case where a creep displacement d_f has occurred on the fault.

$$\left(-\frac{\partial \phi_{\rm pl}}{\partial t} - \mathbf{v}_{\rm s}\cdot\nabla\phi\right) + (1-\phi)\nabla\cdot\mathbf{v}_{\rm s} - \phi\beta_\phi\frac{\partial P_{\rm f}}{\partial t} = 0. \tag{7b}$$

Using the definition of the material derivative, we obtain the conservation equations:

$$\nabla\cdot\left[-\frac{k}{\mu_{\rm f}}(\nabla P_{\rm f} - \rho_{\rm f} g)\right] + \phi\beta_{\rm f}\frac{\partial P_{\rm f}}{\partial t} = -\nabla\cdot(\mathbf{v}_{\rm s}) \tag{8a}$$

$$\frac{1}{1-\phi}\left(-\frac{D\phi_{\rm pl}}{Dt} - \phi\beta_\phi\frac{\partial P_{\rm f}}{\partial t}\right) = -\nabla\cdot(\mathbf{v}_{\rm s}). \tag{8b}$$

In this section, we decomposed the fault core into incompressible grains (or a matrix) and compressible fluids and pores to simplify the calculation of the ductile compaction term. If the grains were allowed to deform, they would bear part of the applied stress. This implies that the calculated pore pressure increase rate is an upper bound. However, the rock mass is not incompressible in the model whenever elastic stresses and deformations are calculated.

The four parameters that need be determined are the total stress, the pore pressure, the porosity and the creep displacement. Eq. (3) gives the compaction rate, eqs (8a) and (8b) give the pore pressure increase rate, and eq. (2) gives the creep displacement. An additional constraint is provided by the total stress in the fault zone:

$$P_{\rm T} = \phi P_{\rm f} + (1-\phi)P_{\rm s}. \tag{9}$$

If we assume that the porosity in faults formed in crystalline rocks is small, then $P_{\rm T} \sim P_{\rm s}$, where $P_{\rm s} = {\rm tr}\,(\sigma)/3$ is the mean stress in the solid. σ_{yy} is known from continuity but σ_{xx} and σ_{zz} are not known. Qualitatively, the temporal changes of $\sigma_{xx} - \sigma_{yy}$ (or $\sigma_{zz} - \sigma_{yy}$) depend on the creeping velocity and should relax back to an initial value if the creeping stops at a rate that depends on both the rigidity of the elastic body and the viscosity of the fault core. If we assume for simplicity that $\sigma_{xx} = \sigma_{zz}$ and defining $\Delta\sigma = \sigma_{xx} - \sigma_{yy}$, a heuristic model for viscous (e.g. elliptical) inclusions in an elastic half-space would give an equation of the form (Y.Y. Podladchikov, private communication, 2002):

$$\frac{d\Delta\sigma}{dt} = C_1 G\frac{\dot{d}_{\rm f}}{L} - C_2\frac{G}{\eta}\Delta\sigma, \tag{10}$$

where C_1 and C_2 are constants depending both on the geometry of the inclusion and on the contrast in elastic modulus and viscosity between the inclusion and the half-space. An interesting follow-on study would be to investigate the total stress field in the ductile core, but is beyond the scope of the current study.

Making the following assumptions, we can use the formalism developed by Sleep & Blanpied (1992): (a) ϕ is small so that $P_{\rm T} \sim P_{\rm s}$ and $1-\phi \sim 1$ in eq. (8b), (b) $\dot{d}_{\rm f} = G\frac{D}{L}\frac{W}{\eta}$, where $D$is the elastic displacement stored in the country rock, (c) all the diagonal elements of the stress tensor are equal to the stress normal to the fault with $P_{\rm s} = \sigma_{\rm n} + 2/3\,\Delta\sigma = \sigma_{\rm n}$ and (d) the fluid is redistributed instantaneously within the fault zone in response to compaction (e.g. pore pressures within the cells are in equilibrium). This last point means that the first term of eq. (8a) describing fluid flow is zero. Numerically, this condition requires high-resolution studies.

Ignoring the details of the velocity distribution within the fault zone, the ductile behaviour of the fault core during interseismic periods is described by

$$\tau = DG/L \tag{11a}$$

$$V = \dot{d}_{\rm f} = \frac{\tau W}{\eta} \tag{11b}$$

$$\frac{d\phi}{dt} = \frac{1}{K}\times(P_{\rm f} - \sigma_{\rm n}) \tag{11c}$$

$$\frac{\partial P_{\rm f}}{\partial t} = -\frac{1}{(\beta_{\rm f}+\beta_\phi)\phi}\frac{D\phi_{\rm pl}}{Dt}, \tag{11d}$$

where τ is the shear stress, G is the elastic modulus, η is the shear viscosity, W is the fault core width, ϕ is its porosity, K is the bulk viscosity, $P_{\rm f}$ is the pore pressure and $\sigma_{\rm n}$ is the normal stress within the fault core and V is the shear creep velocity, i.e. the velocity of one wall of the fault zone with respect to the other wall. For the 3-D case discussed below (Section 3), the shear stress is determined by the solutions of Okada (for a half-space) instead of eq. (11a). In the following, the symbol β will stand for $\beta_{\rm f} + \beta_\phi$. We allow for a small leakage out of the fault zone towards the country rock (via the damage zone high permeability) using a correction term to be added to the rate of pore pressure change in eq. (11d):

$$\left(\frac{\partial P_{\rm f}}{\partial t}\right)_{\rm diff} = -\frac{P_f - P_{\rm h}}{t_{\rm h}}, \tag{12}$$

where $P_{\rm h}$ is the hydrostatic pore pressure in the surrounding rocks and $t_{\rm h}$ is the leak time (Sleep & Blanpied 1992). In principle, fluids could also flow into the fault core if its pore pressure $P_{\rm f}$ was below hydrostatic, but it never happens in our simulations. A simple calculation shows that the ratio between pore pressure increase rates due to compaction and pore pressure decrease rates due to leakage varies between 2 and 25, for high pore pressures or nearly hydrostatic pore pressures, respectively. The calculation was made at 14 km depth, with $P_{\rm f1} = 250$ MPa, $P_{\rm f2} = 150$ MPa, $\sigma_{\rm n} = 400$ MPa, $P_{\rm h} = 137$ MPa, $\phi = 7.4$ per cent and $\eta_{\rm i} = 2.5\times10^{19}$ Pa s (8×10^{11} Pa yr) and $t_{\rm h} = 200$ yr, see eq. (15).

3.1.2 Porosity structure and viscosity coefficients

The porosity of the fault core is made of a wide range of pore shapes, usually represented schematically as the superposition of (micro and macro) cracks and equidimensional pores, and referred to as a double-porosity model. Taking into account these two end-member cases (cracks and spherical pores) in a comprehensive way would require detailed knowledge of the distribution of these cracks and pores (e.g. position, orientation, aperture or aspect ratio). We simplify the problem by rewriting some of the equations derived by Sleep (1995) and Sleep & Blanpied (1992, 1994) concerning creep compaction and frictional dilatancy. As pointed out in SB92, cracks and equidimensional pores behave differently during creep. Sleep & Blanpied (1994) therefore introduce a compaction rate equation for cracks in a medium where pores may also be present, and one for spherical pores in a medium where cracks may also be present (Sleep & Blanpied 1994, eqs 7a and 7b). We advocate that most of the porosity changes relevant to our model are related to cracks (or to subgrain-scale pores that compact as cracks). Therefore, we only consider cracks and adapt their eq. (7a) (written with our notation in eq. 13) to our total porosity model:

$$\frac{\partial f_{\rm c}}{\partial t} = -(\sigma_n - P_{\rm f})\left(\frac{2\alpha_{\rm c} f_{\rm c}}{\eta_{\rm i}}\right)\left(\frac{9+4\alpha_{\rm c} f_{\rm c} + 4 f_{\rm p}}{27+36\alpha_{\rm c} f_{\rm c} + 36 f_{\rm p}}\right), \tag{13}$$

where $f_{\rm c}$ refers to the crack porosity, $\alpha_{\rm c}$ is the crack aspect ratio, $f_{\rm p}$ is the pore porosity and $\eta_{\rm i}$ is the intrinsic viscosity of the grains. The intrinsic viscosity of the grains is a common parameter needed to derive both the shear and the bulk viscosity as motivated by grain-scale physics. At this scale, the nature of the applied stresses (e.g. shear or confining stresses) is not relevant in that both stresses induce a

deformation rate. However, cracks close almost instantaneously at depth, whereas pores compact much more slowly, and the porosity is not zero when all the cracks are closed but is equal to the 'spherical' pore porosity. We introduce a residual porosity $\phi_{\min}$ to account for this behaviour. We also adapt the compaction equation so that the rate reduces rapidly to zero as the porosity approaches this minimum porosity (slow compaction rate for equidimensional pores). We finally assume that: (1) the porosity ranges between $\phi_{\min}$ and a saturation porosity $\phi_{\max}$ (see the next section) and (2) the product of the crack porosity and the crack aspect ratio, present in the viscosity calculation, is equal to 1 for a highly fractured material. The shear viscosity η to be used in eq. (11b) is simplified from SB92, eq. (B1):

$$\eta = \frac{9\eta_{\mathrm{i}}}{13 + 4\phi} \tag{14}$$

and the bulk viscosity K (to be used in eq. (11c) is adapted from Sleep & Blanpied (1994, eqs 7b):

$$\frac{1}{K} = \frac{2}{\eta_{\mathrm{i}}}\left(\frac{13 + 4\phi}{63 + 36\phi}\right)\left(\frac{\phi - \phi_{\min}}{\phi_{\max} - \phi_{\min}}\right)^{a}. \tag{15}$$

The last bracketed term corresponds to a correction term that is close to unity when the porosity is large, and decreases the compaction rate to zero when the cracks are closed. The exponent a controls how fast the compaction rate will decrease when ϕ decreases; the lower the exponent, the faster the decrease will be. Table 1 lists the numerical values chosen for all the model parameters.

Although motivation for this model is derived from subvertical strike-slip faults, Labaume & Moretti (2001) show that both the fault-zone structure and the processes are also found in thrust fault zones. Therefore, our model could be expanded to more complex fault system geometries.

3.1.3 A 3-D case of fault zone without in-plane flow

The first simulation attempts to reproduce the results of Sleep & Blanpied (1992) in a 3-D case. We present results for a 3-D vertical fault zone discretized into sealed subfaults (no in-plane flow, neither coseismic nor interseismic), loaded as described in eq. (11a). Except for the fluid compressibility (we assume constant compressibility, see Table 1) the model parameters are those of SB92 for their Model 1 (see tables 1 and 2 in Sleep & Blanpied 1992). The width W is taken as 1 m, and does not increase with total slip. Fig. 4 shows model results for a cell at 14 km depth for a 500-yr simulation where a steady state is reached. This figure is to be compared with fig. 2 of SB92. The beginning of the simulation, from $t = 0$ to about 60 yr (e.g. the time of the first event) shows a rapid pore pressure increase above hydrostatic, a slow shear stress increase via tectonic loading (top) and a rapid porosity reduction. No significant creep slip has occurred. At the time of the first rupture where the average slip is about 1.5 m, porosity increases from about 8 to 9 per cent by frictional dilatancy. This increase is comparable to increasing 1.3 per cent shown in SB92, but the effect on pore pressure is very different. In the case of constant compressibility, fluid mass conservation yields $P_{\mathrm{new}} = \frac{\phi_{\mathrm{old}}}{\phi_{\mathrm{new}}} \times P_{\mathrm{old}}$, where the subscripts 'old' and 'new' refer to pre- and post-seismic values, respectively.

Fig. 4 shows that pore pressure decreases from about 250 MPa to about 230 MPa, while in SB92 pore pressure drops from 267 MPa down to subhydrostatic levels, 54 MPa. The difference in behaviour rests with the pressure-dependent compressibility. While we agree that pressure-dependent compressibility has an important effect on the post-seismic pore pressure state at great depth and high temperature, when approaching the boiling point, we will argue (and show below) that if the second and third dimensions of the fault zone are considered, pressure-dependent β_{f} plays a secondary role on the actual equilibrated pore pressure. If the compressibility is kept constant, the subfault evolves to a weak (low shear stress), overpressured fault, with a creep slip/seismic slip ratio of about 3 per cent. Consequently, seismic slip occurs every 8.3 yr on average, with much shorter recurrence times than in SB92 (130 yr). The recurrence time is reduced markedly for two reasons. The first one is the already mentioned smaller drop in pore pressure after an event (keeping the frictional strength at a low level). The second one is

Table 1. Model parameters and initial conditions.

Initial model parameters	Range of values
Cell size	2000 m along strike by 500 m up-dip
Fault area	200 km along strike by 18.5 km up-dip
Initial width	10 cm
Basal shear	30 mm yr^{-1} parallel to the plate boundary
Far field compression	3 mm yr^{-1} perpendicular to the plate boundary
Lamé coefficients	$\lambda_{\mathrm{Lamé}} = G = 30 \times 10^9$ Pa
Time step	Time required to initiate failure on exactly one cell
Compressibility $\beta = \beta_\phi + \beta_{\mathrm{f}}$	10^{-3} MPa^{-1}
Initial porosity ϕ	Random between 2 and 7 per cent
Saturation porosity $\phi_{\max}$	Linear with depth between 7 per cent (top) and 3 per cent (bottom)
Residual porosity $\phi_{\min}$	2 per cent
Skempton coefficient B	Random between 0.4 and 0.8
Initial normal stress σ_{n}	Lithostatic, $\rho_r g z$, $\rho_r = 2700$ kg m^{-3}
Initial shear stress	$0.3 \times \sigma_{\mathrm{n}}$
Initial pore pressure gradient	Hydrostatic
Compaction	For $-z < 3$ km, $\dot{\phi} = 0$
	For $-z > 3$ km, creep compaction[a]
Viscosity[b] η_{i}	2.78×10^{11} Pa yr
Bulk viscosity exponent	0.1
Fluid sources $\dot{\Gamma}$	None
Friction coefficients	Static, $\mu_{\mathrm{s}} = 0.6$; dynamic, $\mu_{\mathrm{d}} = 0.5$
Dilatation coefficient[b] r_m	18×10^{-3}

[a] After Sleep & Blanpied (1994).
[b] After Sleep (1995).

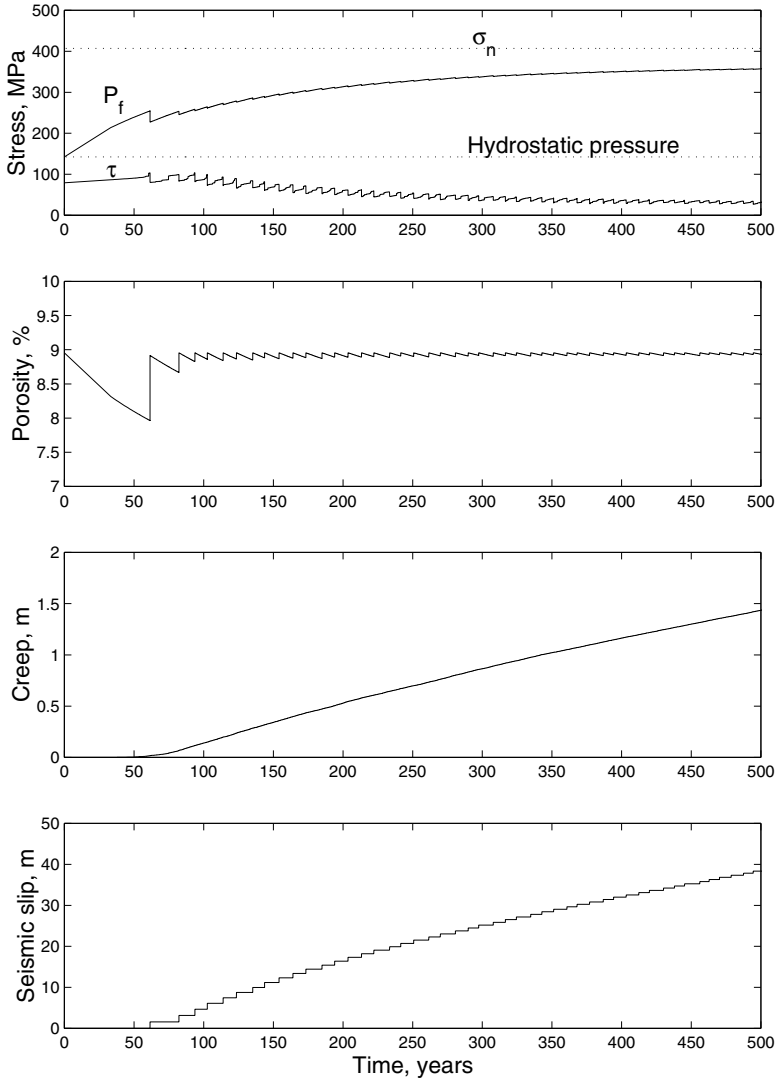

Figure 4. A 3-D case of ductile fault zone without in-plane flow: model results for a cell at 14 km depth for a 500-yr simulation (constant fluid compressibility). From top to bottom: stress state. The two solid lines show the time evolution of shear stress and the pore pressure, whereas the two dotted lines show the hydrostatic and the lithostatic pressure at 14 km depth. Porosity evolution. Creep slip. Seismic slip. Results show first a period of quiescence from $t = 0$ to about 60 yr. Shear stress increases due to tectonic loading, pore pressure increases due to compaction (from 9 to 8 per cent porosity), and no slip has occurred yet. At the time of the first rupture where the average slip is about 1.5 m, porosity increases from 7.96 to 8.91 per cent by frictional dilatancy and pore pressure decreases from about 250 MPa to about 230 MPa, still above the hydrostatic value. The small drop in pore pressure after an event keeps the frictional strength at a low level, leading to a weak fault, with high pore pressure, short seismic cycles (about 8 yr) and low shear stress. The sudden positive steps in shear stress show stress transfer from other cells.

stress transfer from the surrounding subfaults and is seen on the shear stress curve as sudden small increases (steps). This brings the shear stress to the failure stress faster than with tectonic loading alone. Therefore, both the compressibility of the fluid and stress transfer have a significant effect on the resulting behaviour of the viscoelastic fault zone.

4 3-D MODEL

We introduce the ductile fault zone described previously into a 3-D model of faulting. The fault-zone model is coupled to the forward fault interaction model of Fitzenz & Miller (2001). During interseismic periods large-scale tectonic loading increases stresses on the fault and fault compaction increases pore pressures in each sealed subfault. Seismic slip increases porosity by frictional dilatancy and breaks the impermeable seals between subfaults, allowing pore pressure redistribution between the slipped patch and the neighbouring subfaults. Boundary conditions on the model include a basal shear drag and a far-field compression to simulate a transpressional environment. Basal drag is represented by a rectangular dislocation at the base of the model fault moving at constant velocity, and fault normal compression is simulated via an opening mode vertical dislocation. Since pore pressures increase rapidly through ductile compaction, it is very important to consider hydraulic property evolution. Small-scale incremental pore pressure redistribution (see below) avoids great fluid outflows when the ruptures reach the top of the fault. Other changes were made to add features specific for ductile fault zones.

4.1 Interseismic hydraulic property changes

Ductile compaction and leakage out of the fault zone are handled as described in the previous sections. We summarize here the total interseismic pore pressure change rate used in the 3-D model:

$$\frac{\partial P_{\rm f}}{\partial t} = -\frac{(P_{\rm f}-\sigma_{\rm n})}{\beta\phi}\frac{2}{\eta_{\rm i}}\left(\frac{13+4\phi}{63+36\phi}\right)\left(\frac{\phi-\phi_{\rm min}}{\phi_{\rm max}-\phi_{\rm min}}\right)^{a} - \frac{P_f - P_{\rm h}}{t_{\rm h}}. \quad (16)$$

4.2 Coseismic hydraulic property changes

4.2.1 Frictional dilatancy

Seismic slip increases porosity, but whether this frictional dilatancy is a drained or an undrained process is still unclear. For simplicity, we consider that pore pressure actively affects crack propagation in that it lowers the effective stress at the tip of the propagating crack. Hence, although fluids do not fill the new porosity instantaneously, we consider that pore pressure aids the propagation of the cracks responsible for the increase in porosity. Therefore, the energy per fault area ($G_{\rm p}$) required to create porosity will depend on the effective stress and not on the normal stress only, that is, $G_{\rm p} = (\sigma_n - P_{\rm f})W\Delta\phi$ (see Sleep 1995 for a similar approach). On the other hand, the energy released via seismic slip (elastic strain release per fault area) is expressed as $G_{\rm F} = \frac{1}{2}(\tau_{\rm old}D_{\rm old} - \tau_{\rm new}D_{\rm new})$, where $D_{\rm old}$ and $D_{\rm new}$ are recoverable displacements just before and just after the rupture, and $\tau_{\rm old}$ and $\tau_{\rm new}$ are shear tractions for the same two states (Sleep & Blanpied 1994). If we assume that only a small fraction r_m of the seismic energy is available for crack creation (as suggested by Marone *et al.* 1990), then $\Delta\phi \equiv \frac{r_m}{2(\sigma_n - P_{\rm f})W}[\tau_{\rm old}D_{\rm old} - \tau_{\rm new}D_{\rm new}]$. Differentiating with respect to $D_{\rm new}$, we obtain

$$\frac{\partial\phi}{\partial D} \equiv -\frac{r_m\tau}{2(\sigma_n - P_{\rm f})W}, \quad (17)$$

which gives the porosity creation per unit slip. However, as Marone *et al.* (1990) pointed out, the porosity cannot increase via frictional dilatancy beyond a saturation value $\phi_{\rm max}$. We introduce a correction term such that

$$\frac{\partial\phi}{\partial D} \equiv -\frac{r_m\tau}{2(\sigma_n - P_{\rm f})W}\left(\frac{\phi_{\rm max}-\phi}{\phi_{\rm max}}\right), \quad (18)$$

where the term in parentheses keeps the proportionality between the pore creation rate and the faulting energy at low porosity but saturates to $\phi_{\rm max}$. Two additional comments are needed. First, because we use the total porosity and not the crack porosity in eq. (18), we have to introduce a linear depth dependence in $\phi_{\rm max}$ that reflects that the high confining stress would not enable the persistence of crack porosity at depth. The maximum porosities range between 7 per cent at shallow depth (0.5 km) and 3 per cent at greater depth (18 km). The lower bound (3 per cent) corresponds to a maximum of 1 per cent crack porosity and 2 per cent pore porosity. Secondly, since we explicitly monitor $\tau/(\sigma_n - P_{\rm f})$, this term cannot be simply replaced by a friction coefficient. It should be noted that the amount of energy available for crack creation (i.e. $r_m x$ elastic energy) also controls the amount of compaction. The more porosity increases due to slip, the lower the pore pressure becomes and the larger the compaction rate (see eq. 16).

4.2.2 Permeability evolution during slip

As mentioned previously, each cell (or subfault) is initially hydraulically disconnected from the other in-plane cells. Seismic slip can break the in-plane seals. In terms of permeability, this is equivalent to saying that the in-plane permeability of the slipped cells switches from less than 10^{-18} m^2 to about 10^{-15} m^2 over the time step following the event. We consider that at the beginning of the next time step, all subfaults are sealed again. The rate of sealing is a complex problem addressed elsewhere (Gratier *et al.* 2003) but in this simple model, we assume that fault sealing is a rapid process. An additional pore pressure regulation process is a slow diffusive leakage in the direction perpendicular to the fault strike out of the fault core during interseismic periods (Sleep & Blanpied 1992). Little is known concerning the co-seismic connection to the damage zone, but the effect is likely to be very significant (Henderson & Maillot 1997; Gratier *et al.* 2003) and will be discussed in Section 5.

4.2.3 Pore pressure changes

The main issue when dealing with the effects of fluids in fault zones is to evaluate the timescales relevant for each process. Stress transfer occurs at acoustic velocities (of the order of km s^{-1}), while fluid flow is controlled by diffusion. Therefore, in the model, we allow undrained poroelastic effects in response to the changing stress during rupture propagation, which can affect the frictional strength during rupture.

For a diffusion time of less than 3 months (of the order of the time steps) and a permeability of 10^{-15} m^2 (a reasonable co-seismic permeability estimate), the diffusion length is about 2.5 km (Townend & Zoback 2000). Since our cells are 2.0 × 0.5 km^2, we therefore allow the pore pressure of a slipped cell to equilibrate with its nearest neighbours within a time step as a proxy for in-plane diffusion. The equilibrium fluid pressure $\bar{P}_{\rm f}$ among the m affected cells is calculated via

$$\bar{P}_{\rm f} = \frac{\sum_{i=1}^{m}[(\phi\beta W)_i(P_{{\rm f}i} - \rho g\Delta z)]}{\sum_{i=1}^{m}(\phi\beta W)_i} + \rho g\Delta z, \quad (19)$$

where ρ is the fluid density. As previously mentioned, pore and fluid compressibilities are mixed into a single parameter $\beta = \beta_{\rm f} + \beta_\phi$. This equation is different from that of Fitzenz & Miller (2001) because the width of the fault core is neither constant in time (total slip dependence) nor homogeneous in space along the fault. The relative storage capacity of each cell is now explicitly $(\phi\beta\ W(\mathbf{x}))_i$. Conceptually, coseismic flux normal to the fault could be much higher than in-plane flow because of the much larger cross-sectional area, but is not included in the current study. Pore pressure changes are calculated as slip propagates, as described in Miller *et al.* (1999), but this does not feed back on the frictional strength of the fault during the propagation of the event. These changes are monitored but stored and brought back once the stress equilibrium is reached. We assume that by the end of the event, the new cracks created by frictional dilatancy are filled, and we take these porosity changes into account when we calculate the increments of pore pressure redistribution.

When the system reaches equilibrium with respect to its stress state, pore pressures are updated for all the changes listed above and the cells are checked again for frictional failure. In case pore pressure happens to be higher than the minimum principal stress σ_3 at the seal between the fault core and the country rock (e.g. about 90 per cent of the normal stress for the systems investigated so far), we allow hydrofractures to open, draining excess fluid from the overpressured fault core to the drained damaged zone (Scholz 1992). This consists in a drop in pore pressure to just below σ_3, without stress changes, and this pressure drop is assumed to be instantaneous.

4.3 New calculation of time steps

In keeping with our rigorously quasi-static model, the calculation of the time step necessary to fail exactly one cell needs to be determined. To do so, we need to consider the stress path to failure during the interseismic period. Each cell approaches the failure condition by a path determined by the shear stress change rate $\frac{\partial \tau}{\partial t}$, the normal stress change rate $\frac{\partial \sigma_n}{\partial t}$ and the pore pressure change rate $\frac{\partial P_f}{\partial t}$ (Fig. 2). The first two depend on the tectonic loading and on the shear creep, and are dependent on the fault orientation. Pore pressure changes result from both poroelastic effects and viscous compaction.

The introduction of shear creep requires the calculation of a creep velocity for each subfault in the system. Shear creep is a function of shear stress, porosity and width (eq. 11b), and the subsequent stress transfer from each creeping subfault to all subfaults in the model fault system. This makes the time step calculation non-linear and could rapidly become computationally awkward and difficult to manage for large faults or for complicated fault systems. Since many faults are grooved and may slip in only one direction, for simplicity, we consider only the pure strike-slip creep slip. For this case, and for planar faults, we consider that shear creep induces no changes in normal stress. We found that the changes of viscosity with time in the calculation of the shear creep displacement were negligible (i.e. the small effect of the porosity reduction on the viscosity, eq. 14) so that we linearized the calculation of shear stress changes due to shear creep. To calculate the shear stress changes due to shear creep, the stiffness coefficients are calculated using the analytical solutions of Okada (1992), and the creep displacement is obtained from the integration of eq. (11b) with respect to time t. To first order, we obtain a time to failure for each subfault i:

$$\Delta t_i = \frac{-[\tau_i - \mu_s(\sigma_{ni} - p_{fi})]_{\text{init}}}{[sk\tau_i - \mu_s(sk\sigma_{ni} - skp_{fi} - pf_{\text{rate}_i})] + \sum_{j=1}^{n} K_{ij} \frac{W_j}{\eta_j} \tau_j}, \tag{20}$$

where $sk\tau_i$, $sk\sigma_{ni}$ and skp_f refer to increase rates in shear stress, normal stress and pore pressures, respectively, due to tectonic loading (and poroelastic effects). $pf_{\text{rate}i}$ includes both the pore pressure increase rate due to ductile compaction and the decrease due to leakage out of the fault plane (eq. 16) and μ_s is the static friction coefficient. The time step is the minimum of these Δt_i.

4.4 Results of the full 3-D model and interpretation

Fig. 1(a) shows the geometry investigated. To condition the model, we allow 900 yr of tectonic loading (e.g. a stress build-up phase without any seismic or aseismic slip), before creep slip and compaction are initiated on the fault. We monitor the stress and pore pressure state, the seismicity, creep slip, the porosity and the width of the fault zone for each subfault.

4.4.1 Slip on the fault: total seismic slip and total creep slip distributions

Figs 5 and 6 show the state of the fault after about 1000 yr. This time corresponds to a seismic activity of 1500 events, of magnitude ranging from about 4 to 6.5 (with a slope of the frequency–magnitude relationship of about 0.9), and a creep slip of about 5 cm on average at depth.

Each individual seismic rupture shows the strong spatial heterogeneity that was also characteristic in the purely elastic model (Fitzenz & Miller 2001). The cumulative seismic slip distribution is therefore also heterogeneous (Fig. 5a) and the total seismic slip ranges between 1 and 5.5 m. The depth variability of slip is a consequence of the depth-dependent shear stress loading, and slip is non-uniform along strike from the complexity of the stress state on the fault. For an initial fault width of $W_0 = 10$ cm, the width distribution reflects the total slip distribution, with a maximum width of about 30 cm. Eq. (11b) shows the dependence of the shear creep velocity on the fault width. However, it also depends on shear stress. Fig. 5(b) shows the cumulative creep slip distribution, also for $t =$ 1020 yr. The small scale of the heterogeneity of the distribution, as well as the overall increase with depth reflects more the variations in the shear stress distribution (Fig. 6a) than that of the width of the fault core. In this simulation, the intrinsic shear viscosity is 2.5×10^{19} Pa s (8×10^{11} Pa yr) and the creep slip is very small, corresponding to a creep–seismic slip ratio of a maximum of 0.8 per cent. It is of the same order as the ratio obtained by Sleep & Blanpied (1992) for their first simulation. With an intrinsic viscosity of 3.15×10^{19} Pa s (1×10^{12} Pa yr) and a width of $W = 1$ m, they obtained a ratio of 0.2 per cent at 14 km depth. Even though the parameters are not the same, the width-to-viscosity ratios that govern the creep velocity are comparable. In terms of slip behaviour, the two models (1-D and 3-D) are shown to be comparable and mostly seismic.

4.4.2 Pore pressure compartments

The simulation begins with hydrostatic pore pressures throughout the fault plane, and the boundary condition specifies that the fault is mostly sealed except at the top where a constant hydraulic head is applied. This results in a loss of fluid when seismic ruptures reach the surface.

The high initial effective stress from the hydrostatic initial condition results in a high ductile compaction rate (eq. 11c) the only source of pore pressure increase in the model.

Fig. 6(b) shows the evolved pore pressure to normal stress ratio ($\lambda = P_f / \sigma_n$) distribution on the fault plane after about 1000 yr. It has two main features. First, it shows small compartments (of area mostly from two to nine subfaults, so about 6 km along strike by 3 km in depth) compared with the distributions obtained by Fitzenz & Miller (2001) for a similar mean compaction rate (about 3×10^{-5} yr^{-1}). This difference results from the manner in which the new pore pressure state is calculated during the co-seismic propagation of the ruptures. The incremental redistribution used in the present study promotes smaller-scale incremental homogenizations of the pore pressures and avoids a significant cell-size effect. This result is in better accordance with the conclusions of Fenoglio *et al.* (1995) (see the discussion) but how these compartments actually may exist is unknown. A second feature of the model is that the fault is strongly overpressured below 6 km depth. Although the persistence of overpressures at this depth is acceptable in view of field observations or inferences (see the review in Quattrocchi 1999), it is in marked difference with the predictions of the 1-D model of Sleep & Blanpied (1992). In their model, they expect the interseismic pore pressure increase due to ductile compaction to be compensated by the drop in pressure due to co-seismic pore creation (frictional dilatancy). These differences and implications are discussed below.

5 DISCUSSION

5.1 Controls on pore pressure evolution

Adapting the 1-D formalism of SB92 to a 3-D model that includes in-plane coseismic pore pressure redistribution shows contrasting

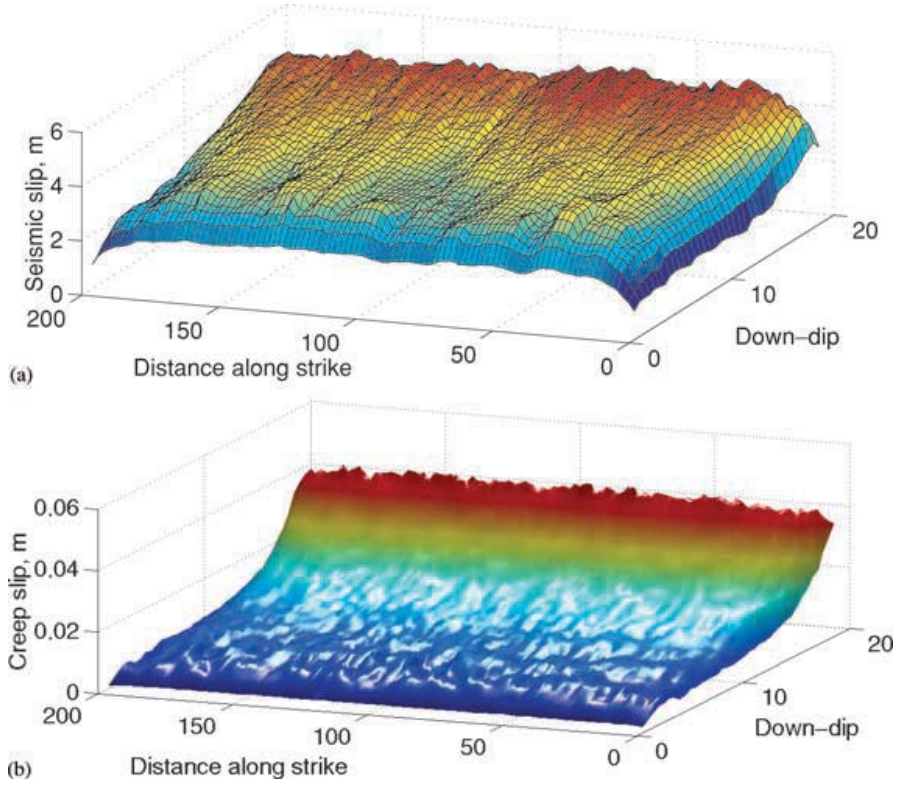

Figure 5. Total displacement on the fault after about 1000 yr. (a) Seismic slip: it ranges from 1 to 5.5 m, with the maximum values reached below 10 km depth. As in Model 1, seismic slip is calculated to induce a drop of 25 per cent of the current shear stress. There is therefore expected to be more slip at depth where the shear stress is the largest (e.g. tectonic loading). The total slip distribution corresponds to about 1500 events with magnitudes ranging from 3.9 to 6.5 and a slope of the frequency–magnitude relationship of about 0.9. (b) Creep slip: the small scale of the heterogeneity of the distribution, as well as the overall increase with depth reflects more the variations in the shear stress distribution (Fig. 6a) than that of the width of the fault core. In this simulation, the intrinsic shear viscosity is 2.78 × 11 Pa yr and the creep slip is extremely small: maximum 5 cm (reached at depths lower than 12 km). This corresponds to a creep–seismic slip ratio of a maximum of 0.8 per cent.

behaviour. In the 1-D formalism, pore pressure changes are controlled by the pressure-dependent compressibility of the fluid. When in-plane processes are considered, this control on the pore pressure state becomes a secondary effect. Section 2.2 made clear that the fluid compressibility controls pore pressure in the 1-D (or sealed subfault) case at depth (with a temperature of about 300 °C, Burnham *et al.* 1969). For a constant compressibility, frictional dilatancy is the only agent of coseismic pore pressure decrease, and is not enough to reduce the pore pressure to hydro- or subhydrostatic levels.

Consider slip on one subfault. If the pore pressure is reduced to hydrostatic (or subhydrostatic) because of pressure-dependent compressibility, then it is still surrounded by a region of near-lithostatically pressured fluid which will diffuse into this coseismically created sink. To illustrate what would happen, consider diffusion of a hydrostatically pressured cell surrounded by its high-pressured neighbours (Fig. 7). For this calculation, numerical values for porosity and pore pressure were taken from SB92 (table 3). The post-seismic porosity of the central cell is 8.7 per cent, and the new pore pressure is hydrostatic (137 MPa at 14 km depth). Influx from the surrounding rock would equilibrate the subhydrostatic 54 MPa calculated by SB92 and the surrounding hydrostatic pore pressure. The porosity of the surrounding cells is 7.4 per cent and the pore pressure is 270 MPa. The cells are 1.0×0.5 km^2. The coseismic hydraulics of the 3-D model is based on the assumption that the seals between the cells break due to seismic slip. Conceptually, we consider that the in-plane permeability switches from a low value (less than 10^{-19} m^2) to a high value of about 10^{-15} m^2. A more accurate description would allow for a decrease in permeability within the cells, as a function of the distance to the boundary with the slipped cell. For small cell sizes, this effect is negligible.

Fig. 7 shows the results of a finite-difference calculation at different times, from 1 to 6 months. We approximate the low permeability outside of the slipped region by a no-flow boundary condition on the four sides of the model. The permeability inside the model is isotropic and is calculated as $k_0\phi^3$ (Brace 1978). We chose $k_0 = 10^{-11}$ m^2 to obtain permeabilities of about 10^{-15} m^2 in the equilibration area. In this calculation, we use the accurate description of the permeability within the cells, i.e. we do not only consider permeabilities at the boundary between the cells as in the model to remove any possible cell-size dependence effect from the conclusions. The results show that after 1 month, the pore pressure already ranges between 190 and 230 MPa in the slipped cell. After 3 months, the pore pressure is almost uniform, above 240 MPa. This value is close to the value of 255 MPa calculated using eq. (19). Reasonably homogeneous pore pressure equilibrium is achieved after about 6 months. This shows that even if the feedback of pressure on compressibility drastically decreases the pore pressure after an earthquake, the importance of this process is reduced when in-plane processes are considered. Since the average t_{step} is of the order of 2–3 months, it also shows that the toggle switch in permeability and our choice of cell size and incremental pore pressure redistribution are consistent

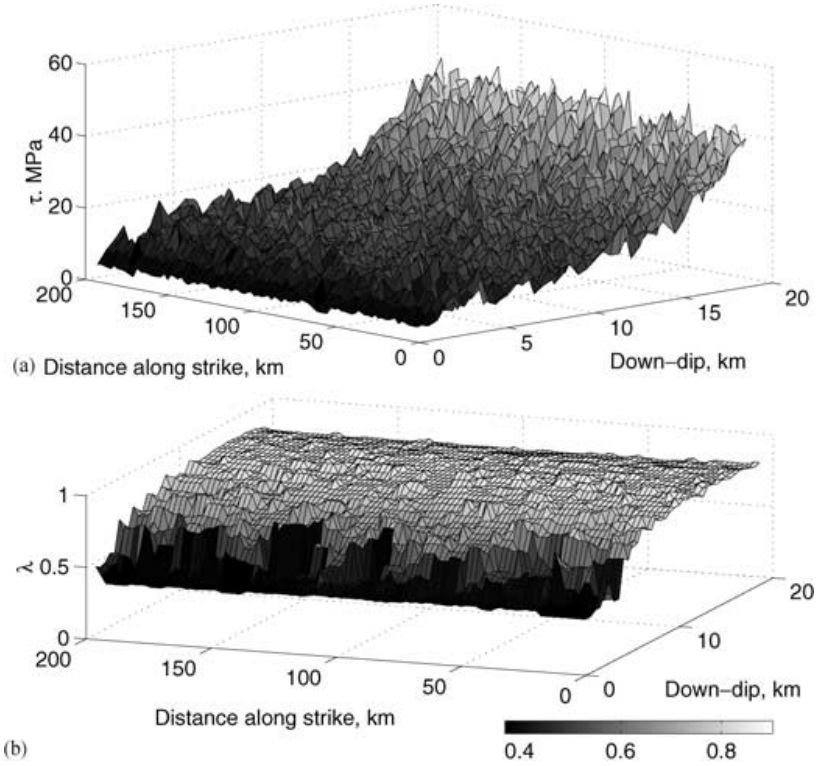

Figure 6. Stress and overpressure state on the fault at $t = 1020$ yr. (a) Shear stress distribution. The distribution shows small-scale heterogeneities, as well as an overall increase with depth due to the tectonic loading, (b) pore pressure to normal stress ratio (λ). The fault is strongly overpressured below 6 km depth and the pore pressure distribution is organized in small compartments.

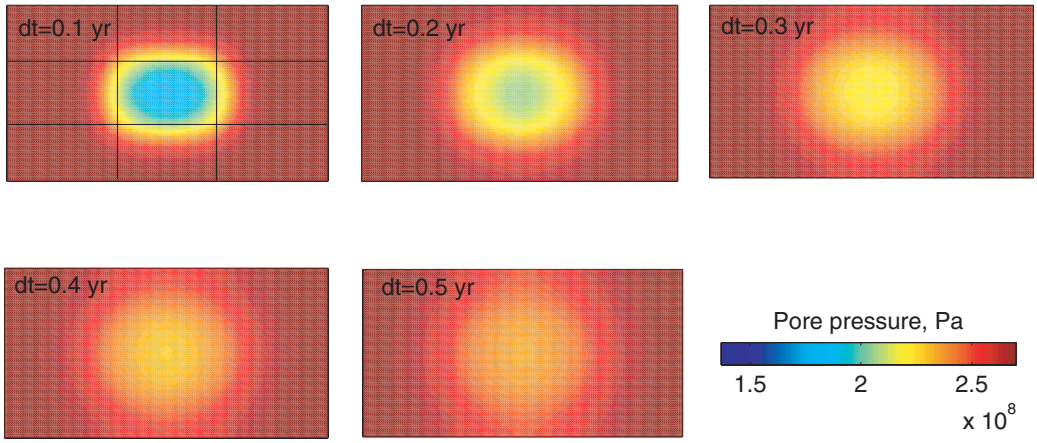

Figure 7. Pore pressure re-equilibration after failure (and dilatancy) of the middle cell. After 3 months, pore pressure is almost uniform, above 240 MPa. This value is close to the 255 MPa calculated with eq. (19). Reasonably homogeneous pore pressure equilibrium is achieved after about 6 months.

with diffusion and does not introduce a significant cell-size effect in the pore pressure distributions.

The ductile compaction mechanism is very efficient at increasing the pore pressure (much more than tectonic loading, compare slopes of $\tau(t)$ and $P_f(t)$ on Fig. 4, top), and rapidly results in overpressured faults. Pore pressure reduction due to seismic slip results in very small changes because of in-plane equilibration. Results from a 3-D fault model (Section 3.4) showed that the frictional strength thus stays low, and that within the time needed to rebuild the shear stress on the fault, the pore pressure increases decrease the Coulomb failure stress, leading to shorter recurrence times for seismic events. The slip distributions of the model seismic events are not homogeneous (e.g. the whole fault plane does not rupture at once), and porosity is increasing only where slip occurred while compaction occurs for every subfault. When a subfault (or a group of subfaults) breaks, the porosity increases, but the seal between this (these) cell(s) and their neighbours also breaks, allowing for pore pressure redistribution. As shown in Fig. 7, the newly created porosity is filled with the fluid excess from the neighbouring (not slipped) cells, impeding a large drop in pore pressure. This phenomenon yields a slow homogenization of the properties of the fault at depth. Later in the simulations, the pore pressure and the slip distributions are very homogeneous.

Although pressure-dependent fluid compressibility has an effect on pore pressure, we conclude that the overpressured behaviour of the fault is mostly a result of the 3-D fault hydraulics. This leads us to conclude that within mostly sealed faults, ductile compaction can only lead to overpressured faults. Although this type of fault exists (e.g. Faulkner & Rutter 2001), it is not a general fault property, so alternative processes accounting for significant flow out of the fault zone are necessary. Potential candidates include the opening of veins and cracks towards the damaged zone that depend on the amount of seismic slip. This idea is supported by field and core observations (Chester *et al.* 1993; Tanaka *et al.* 2001). However, including these processes adds many more unconstrained parameters related to the timescales for the two competing processes: the healing of the cracks and the fluid flow out of the fault core (Gratier *et al.* 2003), and is beyond the scope of this paper.

5.2 Creep slip distribution

Fault creep is observed through measurements of offsets across active faults through time. Wesson (1988) reviews documented partially creeping strike-slip faults, including the San Andreas and the Calavera faults in California and faults in Guatemala, Turkey and China. Offsets of man-made features that cross faults as well as strains, tilts and water level changes in wells have been associated with creep events. The depth to which surface fault creep persists is unclear. Inversion of instrumental tilt and strain measurements, and of short-baseline (<5 km) continuous or frequent line-length measurements, suggest that episodic creep observed at the surface is, in most cases, confined to the uppermost few kilometres or less. On the other hand, aseismic slip is purported to accommodate plate motions at depths greater than the lower limit of earthquake occurrence.

Our model shows a higher creep rate at depth (still within the seismogenic layer) where shear stress is large, than at the surface. The ratio of creep slip to seismic slip at 14 km depth is in accordance with that obtained by SB92. However, the low creep rate near the surface is in disagreement with observations. Because of the low temperatures at shallow depth, thermally activated creep cannot be the mechanism directly responsible for near-surface fault creep. Possible mechanisms for initiating stable slip in the upper 4 km include velocity strengthening as observed in laboratory friction experiments when slip is forced to occur within a thick gouge (Marone & Scholz 1988). If natural faults contain a thick unconsolidated gouge within their shallow regions, they may exhibit stable slip within those regions and unstable slip below the depth at which the gouge becomes consolidated/indurated (and possibly thinner). For well-developed faults, comparisons of afterslip distribution (confined to the upper 3 km) and hypocentre distributions (4–14 km) are consistent with velocity strengthening at shallow depth, acting to arrest coseismic slip, resulting in a slip deficit that, upon relaxation, produces afterslip (e.g. 1979 Imperial Valley earthquake, Marone & Scholz 1988). For poorly developed faults, seismic slip occurs throughout the upper 6 km (see the review in Marone & Scholz 1988). In the near-surface region, the confining stress is low, resulting in lower grain contact areas than at depth, even for high roughness. This results in low peak strength (Barton 1976) and large grain size in the fault gouge. This could be accounted for by a lower intrinsic viscosity (Sleep & Blanpied 1992).

A possible model improvement would be to add a dependence of the fault width–total slip relationship on confining stress (or depth) to obtain thicker fault zones in the upper part of the fault zone, and a dependence of the intrinsic viscosity η_i on the total slip (e.g. accounting for grain-size diminution with slip or with depth). Another limitation of the model is related to the already mentioned limited role of the damage zone explicitly plugged into the model. Li & Vidale (2001) and Li *et al.* (2001) studied the velocity of the guided waves on the Landers fault and the exhumed Punchbowl fault, respectively, showing a decrease from 10 to 50 per cent (10–25 per cent for the Punchbowl fault) within the waveguide width (*ca.*200 m for Landers, tens of metres for the Punchbowl fault) compared with the wall-rock values. They attribute this low-velocity zone as being a remnant of the process zone formed by inelastic deformation around the propagating crack tip during dynamic rupture. Li *et al.* (2001) calculate fracture density profiles across the fault zone and show the relationship between the effective shear modulus, Poisson's ratio and the fracture density. They show a gradual reduction in velocity (i.e. a gradual reduction in shear modulus and an increase in crack density) from the outer boundaries inward to a central velocity minimum (their Fig. 7). If we explicitly introduced the damage zone and the low-shear modulus zone associated with it, this could alter the creep rate as calculated in eq. (2). However, the kinematics of the system behaviour depend on the ratio G/η, and other factors being equal, η may be selected to produce a given long-term slip rate $\dot{d}_f$ in eq. (2). More fundamentally, it can be shown that far-field deformation (both displacement and stress) depends on potency (slip integrated over the slip area, see the review in Ben-Zion 2001) rather than seismic moment (Ben-Zion 1989; Heaton & Heaton 1989). This means that at interaction distances much larger than the width of the low rigidity zone (e.g. the fault and damaged zone), the deformation field resulting from an imposed slip within the ductile fault zone will not depend on *G*at the source.

6 CONCLUSION AND PERSPECTIVES

We presented a 3-D forward fault model including tectonics, fluids and stress transfer for ductile fault zones. Model faults have the properties of fault cores and are viscoelastic thin (decimetre to metre scale) vertical ductile bodies embedded in an elastic half-space and hydraulically isolated from the surrounding rocks by a narrow near-impermeable seal (a small leakage term is allowed). The conceptual model includes a simplification of the double-porosity model described by Sleep & Blanpied (1992). We introduced the 1-D formalism for ductile compaction and shear creep into the model of Fitzenz & Miller (2001), and showed that the fluid compressibility is the dominant effect controlling pore pressure changes in the close-to-1-D case. In the 3-D model, slip on the fault is accounted for by viscous shear creep during interseismic periods and seismic slip when the Coulomb failure stress criterion is met. The hydraulic properties of the fault are determined by viscous compaction and frictional dilatancy (for porosity) and a toggle switch in-plane permeability allows for pore pressure redistribution after seismic events (Miller & Nur 2000). We found that whatever fluid compressibility law we choose, model faults submitted to shear creep and ductile compaction will tend to develop overpressured compartments at depth (below 6 km), because of the heterogeneous slip distributions and in-plane coseismic flow within slipped patches (slipped cells and their neighbours).

We made a number of assumptions to derive the system of equations needed to handle the inclusion of a viscoelastic fault core in an elastic half-space, but more theoretical work is required to obtain a more general set of equations. The total stress P_T in a ductile layer should be determined analytically or numerically and should include a dependence on shear creep velocity.

The parameters used in our model are poorly constrained (porosities, intrinsic viscosity, fraction of the energy that goes into crack creation, width–slip relationship), revealing the need for more laboratory and field work.

Another issue is how fault-zone structures evolve at depth (4–15 km). The structure chosen here is based on observations of the rocks taken from the Nojima fault zone. The depth reached by the boreholes is of the order of 1 km. What would be the picture at greater depth? We know from observations of vein fields (deemed related to faulting episodes that occurred at depths in the range 6–10 km, Cox 1995) and exhumed fault zones that the processes (shear creep, evidence for high pore pressures, as well as coseismic dilatancy) are the same (see the review by Sleep & Blanpied 1992), but what about the width, the porosity and the permeability of each part of the fault zone? Moore *et al.* (1999) wrote 'fault motion may shift to a completely new strand, leaving the old strand outside the damage zone of the new one' and in this case the old gouge layer would be gradually sealed. In contrast, if the new site of localized shear stress is within the same fault strand, then 'the old gouge layer would be limited to dilational fracturing and minor shearing'. It would therefore be interesting to reset from time to time, randomly, the porosity to high initial values in the code to simulate a shift to a completely new strand. An additional point is aimed at emphasizing the need for a collection of models: all faults do not have this architecture (Rawling *et al.* 2001).

A final note. Since many faults have very long recurrence times, the overpressured faults easily activated in this model suggest that the out-of-plane hydraulics need to be understood and probably play a crucial role in the pore pressure regulation.

It remains to be seen whether these new hydraulic features, coupled both to a better evaluation of the role of the damaged zone in the pore pressure cycles and to the evolution of fault systems following the evolution of the principal stresses (dynamic fault generation), can lead to realistic fault behaviour within the framework of a regional model.

ACKNOWLEDGMENTS

The authors thank Mike Blanpied for many insightful comments on an early version of the manuscript, Keith Evans, Dave Lockner, Nick Beeler, Fred Pollitz and Jim Dieterich for stimulating discussions or comments, Yuri Podladchikov for a decisive theory afternoon, and Norm Sleep for clarifying parts of his model. Reviews by Professors Borm and Sleep improved the manuscript. This research was supported by the Swiss National Fund, programme 2100-054121.98/1.

REFERENCES

Argus, D.F. & Gordon, R.G., 1991. Current Sierra Nevada–North America motion from very long baseline interferometry: implications for the kinematics of the western United States, *Geology,* **19,** 1085–1088.

Barnes, H.A., Hutton, J.F. & Walters, K., 1993. *An Introduction to Rheology,* Vol. 3 of Rheology series, Elsevier, Amsterdam.

Barton, N., 1976. The shear strength of rock and rock joints, *Int. J. Rock Mech. Min. Sci. Geomech. Abtr.,* **13,** 255–279.

Ben-Zion, Y., 1989. The response of two joined quarter spaces to, *SH* line sources located at the material discontinuity interface, *Geophys. J. Int.,* **98,** 213–222.

Ben-Zion, Y., 2001. On quantification of the earthquake source, *Seismol. Res. Lett.,* **72,** 151–152.

Ben-Zion, Y. & Rice, J.R., 1993. Earthquake failure sequences along a cellular fault zone in a three-dimensional elastic solid containing asperity and nonasperity regions, *J. geophys. Res.,* **98**, 14 109–14 131.

Blanpied, M.L., Lockner, D.A. & Byerlee, J., 1992. An earthquake mechanism based on rapid sealing of faults, *Nature,* **358**, 574–576.

Blanpied, M.L., Tullis, T.E. & Weeks, J.D., 1998. Effects of slip, slip rate, and shear heating on the friction of granite, *J. geophys. Res.,* **103**, 489–511.

Brace, W.F., 1978. A note on permeability changes in geologic material due to stress, *Pure appl. Geophys.,* **116,** no. 4–5, 627–633.

Burnham, C., Holloway, J. & Davis, N., 1969. *Thermodynamic Properties of Water to 1000 °C and 10 000 Bars,* p. 96, Geological Society of America, Boulder, Colorado.

Chester, F.M., Evans, J.P. & Biegel, R.L., 1993. Internal structure and weakening mechanisms of the San Andreas fault, *J. geophys. Res.,* **98**, 771–786.

Cox, S.F., 1995. Faulting processes at high fluid pressures: an example of fault valve behaviour from the Wattle Gully fault, Victoria, Australia, *J. geophys. Res.,* **100**, 12 841–12 859.

Faulkner, D.R. & Rutter, E.H., 2001. Can the maintenance of overpressured fluids in large strike-slip fault zones explain their apparent weakness?, *Geology,* **29**, 503–506.

Fenoglio, M.A., Johnston, M.J.S. & Byerlee, J.D., 1995. Magnetic and electric fields associated with changes in high pore pressure in fault zones: application to the Loma Prieta ULF emissions, *J. geophys. Res.,* **100**, 12 951–12 958.

Fitzenz, D.D. & Miller, S.A., 2001. A forward model for earthquake generation on interacting faults including tectonics, fluids, and stress transfer, *J. geophys. Res.,* **106**, 26 689–26 706.

Gratier, J.-P., Favreau, P. & Renard, F., 2003. Modeling fluid transfer along Californian faults when integrating pressure solution crack-sealing and compaction processes, *J. geophys. Res.,* **108**, 2104–2129.

Harris, R.A. & Day, S.M., 1999. Dynamic 3D simulations of earthquakes on en echelon faults, *Geophys. Res. Lett.,* **26**, 2089–2092.

Heaton, T.H. & Heaton, R.E, 1989. Static deformations from point forces and force couples located in welded elastic poissonian half-spaces: implications for seismic moment tensors, *Bull. seism. Soc. Am.,* **79**, 813–841.

Henderson, J.R. & Maillot, B., 1997. The influence of fluid flow in fault zones on patterns of seismicity: a numerical investigation, *J. geophys. Res.,* **102**, 2915–2924.

Honkura, Y. *et al.*, 2000. Preliminary results of multidisciplinary observations before, during and after the Kocaeli (Izmit) earthquake in the western part of the north Anatolian fault zone, *Earth Planets Space,* **54**, 293–298.

Labaume, P. & Moretti, I., 2001. Diagenesis-dependence of cataclastic thrust fault zone sealing in sandstones. Example from the Bolivian sub-andean zone, *J. Struct. Geol.,* **23**, 1659–1675.

Li, Y.-G. & Vidale, J.E., 2001. Healing of the shallow fault zone from 1994–1998 after the 1992 *M*7.5 Landers, California, earthquake, *Geophys. Res. Lett.,* **28**, 2999–3002.

Li, Y.-G, Vidale, J.E., Aki, K., Xu, F. & Burdette, T., 1998. Evidence of shallow fault zone strengthening after the 1992 *M* 7.5 Landers, California, earthquake, *Science,* **279**, 217–219.

Li, Y.-G., Chester, F.M. & Vidale, J.E., 2001. Shallow seismic profiling of the exhumed Punchbowl fault zone, Southern California, *Bull. seism. Soc. Am.,* **91**, 1820–1830.

Marone, C. & Scholz, C.H., 1988. The depth of seismic faulting and the upper transition from stable to unstable slip regimes, *Geophys. Res. Lett.,* **15**, 621–624.

Marone, C., Raleigh, C.B. & Scholz, C.H., 1990. Frictional behavior and constitutive modeling of simulated fault gouge, *J. geophys. Res.,* **95**, 7007–7025.

Miller, S.A. & Nur, A., 2000. Permeability as a toggle switch in fluid-controlled crustal processes, *Earth planet. Sci. Lett.,* **183**, 133–146.

Miller, S.A., Nur, A. & Olgaard, D.L., 1996. Earthquakes as a coupled shear stress-high pore pressure dynamical system, *Geophys. Res. Lett.,* **23**, 197–200.

Miller, S.A., Ben-Zion, Y. & Burg, J.-P., 1999. A three dimensional fluid-controlled earthquake model: behavior and implications, *J. geophys. Res.,* **104**, 10 621–10 638.

Moore, D.E., Lockner, D.A., Ito, H. & Ikeda, R., 1999. Correlation of deformation textures with laboratory measurements of permeability and

strength of Nojima fault zone core samples, in Proc. Int. *Workshop on the Nojima Fault Core and Borehole Data Analysis,* pp. 159–166, USGS Open-file report 00-129.

Morrow, C. & Byerlee, J., 1989. Experimental studies of compaction and dilatancy during frictional sliding on faults containing gouge, *J. Struct. Geol.,* **11**, 815–825.

Okada, Y., 1985. Surface deformation due to shear and tensile faults in a half-space, *Bull. seism. Soc. Am.,* **75**, 1135–1154.

Okada, Y., 1992. Internal deformation due to shear and tensile faults in a half space, *Bull. seism. Soc. Am.,* **82**, 1018–1040.

Pollitz, F.F., Wicks, C. & Thatcher, W., 2001. Mantle flow beneath a continental strike-slip fault: postseismic deformation after the 1999 Hector Mine earthquake, *Science,* **293**, 1814–1818.

Quattrocchi, F., 1999. In search of evidence of deep fluid discharges and pore pressure evolution in the crust to explain the seismicity style of the Umbria-Marche 1997–1998 seismic sequence (central Italy), *Ann. Geofis.,* **42**, 609–636.

Rawling, G.C., Goodwin, L.B. & Wilson, J.L., 2001. Internal architecture, permeability structure, and hydrologic significance of contrasting fault-zone types, *Geology,* **29**, 43–46.

Renard, F., Gratier, J.-P. & Jamtveit, B., 2000. Kinetics of crack-sealing, intergranular pressure solution, and compaction around active faults, *J. Struct. Geol.,* **22**, 1395–1407.

Rice, J.R., 1992. Fault stress states, pore pressure distributions, and the weakness of the San Andreas fault, in *Fault Mechanics and Transport Properties of Rocks,* Vol. 51, pp. 9885–9907, eds Evans, B. & Wong, T.-f, *Int. Geophys. Ser.*, Academic, San Diego

Robinson, R. & Benites, R., 1995. Synthetic seismicity models of multiple interacting faults, *J. geophys. Res.,* **100**, 18 229–18 328.

Robinson, R. & Benites, R., 1996. Synthetic seismicity models for the Wellington region, New Zealand: implications for the temporal distributions of large events, *J. geophys. Res.,* **101,** 27 833–27 844.

Scholz, C.H., 1990. *The Mechanics of Earthquakes and Faulting,* Cambridge Univ. Press, New York.

Scholz, C.H., 1992. Weakness amidst strength, *Nature,* **359**, 677–678.

Segall, P. & Rice, J.R., 1995. Dilatancy, compaction, and slip instability of a fluid-infiltrated fault, *J. geophys. Res.,* **100**, 22 155–22 171.

Sibson, R.H., 1992. Fault-valve behavior and the hydrostatic-lithostatic fluid pressure interface, *Earth Sci. Rev.,* **32**, 141–144.

Sleep, N., 1995. Ductile creep, compaction and rate and state dependent friction within major fault zones, *J. geophys. Res.,* **100**, 13 065–13 080.

Sleep, N. & Blanpied, M.L., 1992. Creep, compaction and the weak rheology of major faults, *Nature,* **359**, 687–692.

Sleep, N. & Blanpied, M.L., 1994. Ductile creep and compaction: a mechanism for transiently increasing fluid pressure in mostly sealed faults zones, *Pure appl. Geophys.,* **143**, 9–40.

Stein, R.S., Barka, A.A. & Dieterich, J.H., 1997. Progressive failure on the North Anatolian fault since 1939 by earthquake stress triggering, *Geophys. J. Int.,* **128**, 594–604.

Tanaka, H., Fujimoto, K., Ohtani, T. & Ito, H., 2001. Structural and chemical characterization of shear zones in the freshly activated Nojima fault, Awaji island, southwest Japan, *J. geophys. Res.,* **106**, 8789–8810.

Townend, J. & Zoback, M.D., 2000. How faulting keep the crust strong, *Geology,* **28**, 399–402.

Ward, S.N., 1997. Dogtails versus rainbows: synthetic earthquake rupture models as an aid in interpreting geological data, *Bull. seism. Soc. Am.,* **87**, 1422–1441.

Wesson, R.L., 1988. Dynamics of fault creep, *J. geophys. Res.,* **93**, 8929–8951.

Wibberly, C.A.J. & Shimamoto, T., 2003. Internal structure and permeability of major strike-slip fault zones: the Median Tectonic Line in Mie prefecture, southwest Japan, *J. Struct. Geol.,* **25**, 59–78.

Yamashita, T., 1998. Simulation of seismicity due to fluid migration in a fault zone, *Geophys. J. Int.,* **132**, 674–686.

Yamashita, T., 1999. Pore creation due to fault slip in a fluid-permeated fault zone and its effect on seismicity: generation mechanism of earthquake swarms, *Pure appl. Geophys.,* **155**, 625–647.

Zhang, S., Tullis, T. & Scruggs, V., 2001. Implications of permeability and its anisotropy in a mica gouge for pore pressures in fault zones, *Tectonophysics,* **335**, 37–50.